SANDIA REPORT

SAND2008-6125
Unlimited Release
Printed September 2008

Terahertz-Based Target Typing

Eric A. Shaner, Todd Barrick, Albert D. Grine, Sungkwun K. Lyo, John L. Reno, and Michael C. Wanke

Prepared by
Sandia National Laboratories
Albuquerque, New Mexico 87185 and Livermore, California 94550

Sandia is a multiprogram laboratory operated by Sandia Corporation, a Lockheed Martin Company, for the United States Department of Energy's National Nuclear Security Administration under Contract DE-AC04-94AL85000.

Issued by Sandia National Laboratories, operated for the United States Department of Energy by Sandia Corporation.

Available to DOE and DOE contractors from
U.S. Department of Energy
Office of Scientific and Technical Information
P.O. Box 62
Oak Ridge, TN 37831

Telephone: (865) 576-8401
Facsimile: (865) 576-5728
E-Mail: reports@adonis.osti.gov
Online ordering: http://www.osti.gov/bridge

Available to the public from
U.S. Department of Commerce
National Technical Information Service
5285 Port Royal Rd.
Springfield, VA 22161

Telephone: (800) 553-6847
Facsimile: (703) 605-6900
E-Mail: orders@ntis.fedworld.gov
Online order: http://www.ntis.gov/help/ordermethods.asp?loc=7-4-0#online

SAND2008-6125
Unlimited Release
Printed September 2008

Terahertz-Based Target Typing

E.A. Shaner and S.K. Lyo
Semiconductor Material and Device Sciences Department

J.L. Reno
CINT Scientist

Todd Barrick, A.D. Grine, and M.C. Wanke
Photonic Microsystems Technology

Sandia National Laboratories
P.O. Box 5800
Albuquerque, New Mexico 87185-MS1415

Abstract

The purpose of this work was to create a THz component set and understanding to aid in the rapid analysis of transient events. This includes the development of fast, tunable, THz detectors, along with filter components for use with standard detectors and accompanying models to simulate detonation signatures. The signature effort was crucial in order to know the spectral range to target for detection. Our approach for frequency agile detection was to utilize plasmons in the channel of a specially designed field-effect transistor called the grating-gate detector. Grating-gate detectors exhibit narrow-linewidth, broad spectral tunability through application of a gate bias, and no angular dependence in their photoresponse. As such, if suitable sensitivity can be attained, they are viable candidates for Terahertz multi-spectral focal plane arrays.

CONTENTS

NOMENCLATURE

2DEG	Two-Dimensional Electron Gas
DC	Direct Current
DOE	Department of Energy
DXRL	Deep X-Ray Lithography
FEL	Free Electron Laser, a widely tunable laser radiation source
FET	Field Effect Transistor
FWHM	Full Width at Half Maximum
LED	Light Emitting Diode
LIGA	a German acronym for **Li**thographie, **G**alvanoformung, **A**bformung," in English (X-ray) Lithography, Electroplating, and Molding
NEP	noise equivalent power
SNL	Sandia National Laboratories
SNR	Signal-to-Noise Ratio
SPP	Surface Plasmon Polariton
QW	Quantum Well
THz	Terahertz, 10^{12}Hz

1. BACKGROUND

1.1. Motivation

There has been increased interest in the terahertz (THz, 10^{12}Hz) portion of the spectrum, particularly in the past 5-10 years, for a variety of security and sensing related applications. In this particular work, detection speed, sensitivity, and wavelength selectivity are all desired. Combined with this, is the additional challenge of needing to understand what spectroscopic signatures to expect from transient events in order to know approximately 'where to look' in frequency.

1.2. Semiconductor Plasmons

Our detectors are based on two-dimensional plasmons in the channel of a field effect transistor (FET). Semiconductor plasmons are simply a charge oscillation having natural oscillation frequencies that depend on the carrier density. In a doped bulk (3-dimensional) semiconductor, it is well known that the plasma frequency is given by $\omega_p^2 = ne^2 / \varepsilon\varepsilon_0 m^*$. Where n is the carrier concentration, e is the charge of an electron, $\varepsilon\varepsilon_0$ is the background dielectric constant of the semiconductor, and m^* is the effective electron mass in the semiconductor. When the semiconductor system is reduced to two-dimensions, as in the channel of a field effect transistor, the screening dynamics are changed as charge electric field lines can fringe outside of the 2D layer. The end result is that the plasmon frequency now has a dispersion relation given by[1]:

$$\omega_p^2 = \frac{e^2 n(V_G) k}{2\varepsilon\varepsilon_0 m^*} \qquad (1.1)$$

where $n(V_G)$ is the 2D carrier density at a gate bias V_G, k is the plasmon wave vector, *and* $_p$, e, $\varepsilon\varepsilon_0$, and m^* are as previously defined. The presence of a gate metal above the transistor channel modifies the basic relation of equation 1.1 yielding[2]:

$$\omega_p^2 = \frac{e^2 n(V_G) k}{\varepsilon\varepsilon_0 (1+\coth(kd)) m^*} \qquad (1.2)$$

Here d is the distance between the 2D transistor channel, and the gate metal. This typically results in a minor correction to the plasmon frequency, so in general throughout this document, equation 1.1 will be used for plasmon frequency calculations.

The most notable aspect of the plasmon dispersion relation is that frequency is proportional to the square root of both density and wave vector. This relation is used to identify plasmons as the resonant mechanism that is responsible for the photoresponse in grating-gate detectors. Typical electron densities of 10^{10} to 10^{12} cm^{-2} and device geometries of several microns in high-mobility systems lead to plasmon modes in the ~ 1 THz range. This is where coupling to 2D plasmons can be seen as problematic. Typical THz wavelengths are on the order of several hundred microns, whereas the corresponding

plasmon wavelengths are on the order of microns. The resulting severe wavevector (2 /λ) mismatch means that radiation does not naturally couple to the plasmons. However, the use of a grating, with a period matched to the plasmon wavelength, spatially modulates the incident radiation and permits coupling of THz radiation to plasmon modes[3]. While this technique was applied almost three decades ago in order to observe 2D plasmons in semicondcutors[3], to date, we have yet to see truly useful photodetectors based on these principles.

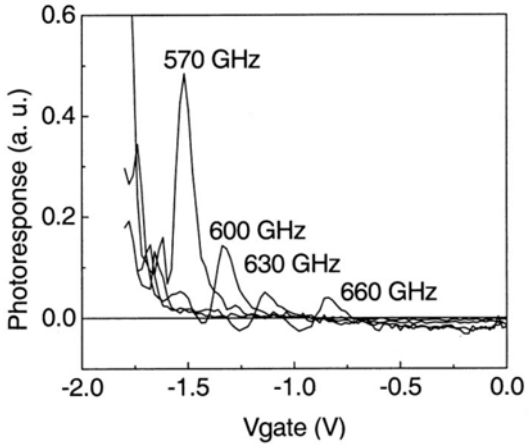

Fig. 1.1: Photoresponse of a double quantum well grating gate detector to different frequencies radiation. As the gate bias is changed, the frequency of the plasmon resonance in the device changes. When there is a match between the plasmon frequency and the radiation frequency, a peak is seen in the photoresponse.

1.3: Work prior to this LDRD

As mentioned in section 1.2, many years prior to our work, 2D semiconductor plasmons had been observed[3]. In 2002, a double quantum well grating-gate detector had been demonstrated, in a collaboration between Sandia and UCSB[4]. This detector was shown to have a voltage tunable photoresponse[4] as demonstrated in fig. 1.1.

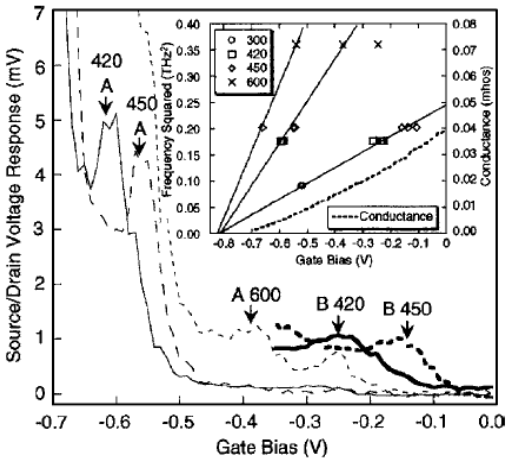

Fig. 1.2: Photoresponse of single-quantum well grating gate detectors. Inset shows a mode map which proves the excitations are quantum well plasmons.

While the tunable photoresponse was a nice result, the noise equivalent power (NEP) was only 10^{-5}W/ Hz, 5 orders of magnitude worse than where it is desired to be. Beyond this, the dynamics underlying the photoresponse were not understood. Corresponding measurements done at the time also indicated that the double quantum well (as opposed to a single quantum well which is closer to a standard field effect transistor) was absolutely necessary in order to observe a photoresponse.

In a related LDRD effort prior to this project, it was found that grating-gate detectors made from single-quantum well material functioned in a similar way to the double-quantum well[5]. This realization helped lay the ground for the work performed under this project. The data of Fig 1.2 illustrates the resonant photoresponse in a single well grating-gate detector at different illumination frequencies. The inset of

fig. 1.2 shows a mode map created by plotting resonant peak photoresponse positions. The slopes of the lines intersecting the data points closely match a 1:3:5 ratio. Combined with fitting reasonable parameters using Eq. 1.1, this proves that the photoresponse is due to plasmon excitations in the single quantum well[2].

2. ACCOMPLISHMENTS

2.1: Determination of Frequencies of Interest

Since it is desired to create an array of detectors each tuned to a separate frequency for the purpose of identifying molecular constituents in a vapor cloud, we want to know roughly where the detectors should be tuned and how sensitive these detectors need to be. Thus we modeled the emission spectra that would occur from the gaseous by-products of the detonation of Comp-B. Modeling codes for emission from hot gasses are not available in this frequency range. This being the case, we calculated the absorption for a typical experimental path length, converted this to an effective pressure- and temperature-dependent absorptivity, assumed thermal equilibration, and equated the absorptivity to emissivity so we could calculate the expected emission of the byproducts for two separate temperatures (278K and 1000K). The expected power incident on a detector assuming optics compatible with the experiments and a gas temperature of 278K is shown as a function of frequency in Fig. 2.1. The emission for a gas at 1000K is nearly the same below 50 cm^{-1}. This is a consequence that in gases the occupation of states shifts with temperature which counteracts the expected increase in emission at higher temperatures. Below 30 cm^{-1}, the separation between lines is large enough that our devices can resolve their separation. However, higher resolution detectors are needed to use the stronger signals above 30 cm^{-1} where more accurate identification is possible.

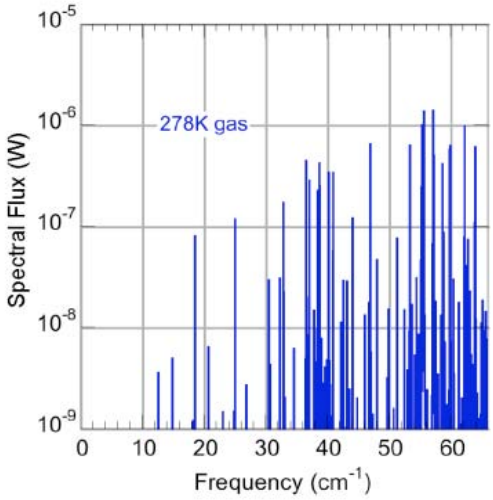

Fig. 2.1: Calculated power collected by a 2 inch aperture, F/2 system from emission lines of the by-products of Comp-B detonation.

In the first year of this project, detonation shots of comp-B were performed. The details of these shots are documented in a previous sand report (SAND2007-0835). While the grating-gate detectors were employed in these measurement, tuned to a frequency of 800 GHz, it was determined after analysis, that the detectors needed improved sensitivity in order to be useful for future characterization of such events. This being the case, the remainder of this project focused on improving detector sensitivity as well as creating passive filtering components for use with mature, yet broadband, THz detectors such as Silicon and Niobium bolometers.

2.2 LIGA fabricated THz waveguide filter

Development of a high pass THz waveguide filter can enable some spectroscopic information to be obtained from broadband detectors. These filters were designed specifically to reduce the excess surface plasmon-polariton (SPP) mode associated with the Wood's anomaly present in thin metallic filters[6]. These signals often represent a

large amount of the power transmitted through the filter. Furthermore, SPP modes are close enough to the primary mode to distort the general cutoff of the filter and reduce the ability to detect specific signals in a tight wavelength band.

Numerical calculations based on formalisms developed by Chen[7] and Winnewisser[8] show that that increasing the thickness of the filter significantly increases the quality factor of the filter. Figure 2.2 shows the expected transmission spectrum of a 35 m circular hole filter in a close pack array with a pitch of 45 m. Each line represents a different filter thickness. As the thickness of the filter increases it demonstrates a sharper low frequency cutoff. Further more, work by Genet[9] shows that the transmission of surface plasmons through a sub wavelength waveguide filter is decreased as the thickness of the filter increases. The exact transmission coefficients are still being investigated. However by fabricating a 500 m tall THz filter, we can effectively prevent the transmission of surface plasmons observed in all thin sub wavelength filters.

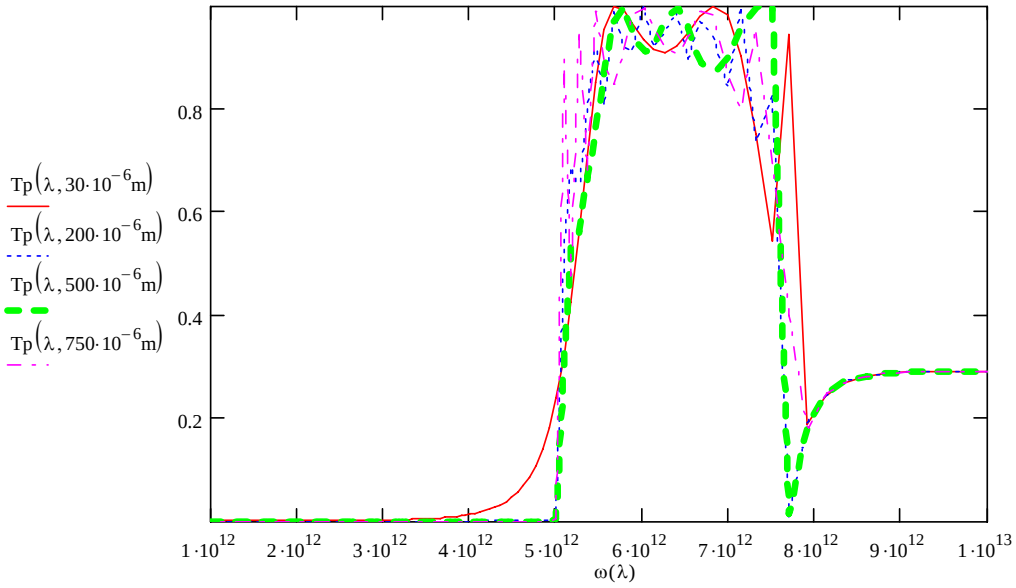

Fig. 2.2: Real Component of the transmission through the filter vs. frequency as a function of filter thickness (30 μm, 200 μm, 500 μm, and 750 μm).

To overcome this issue, the filters were fabricated using the LIGA technique (LIGA is a German acronym, it refers to the use of high aspect ratio lithography, combined with electroplating) to increase the overall aspect ratio of patterned waveguides in a metallic block. Previous efforts in LIGA THz devices have focused on the ability to create passive THz devices using structures with aspect ratios less than 40:1[10,11]. While these structures yield acceptable results, they do not demonstrate the metal pattern requirements for effectively eliminating the second transmission mode in THz filters. We have designed a filter with a 30-40 m hole size, and a wall thickness of 10 m, capable of filtering light greater than outside of the 30-60 m band width. Furthermore, we have improved our processing capability illustrated in fig 2.3 to demonstrate filters with structural aspect ratios up to 100:1. Thus, we are now able to produce high tolerance THz filters 500 m and 750 m tall that effectively eliminate the Wood's

anomaly from our transmission signal. Initial structures were completed using existing Deep X-ray Lithography (DXRL) test masks and were subsequently too small to make accurate spectroscopic measurements on. We have made complete $1cm^2$ area filters that were tested using a THz photomixer source (see sec. 2.3.2).

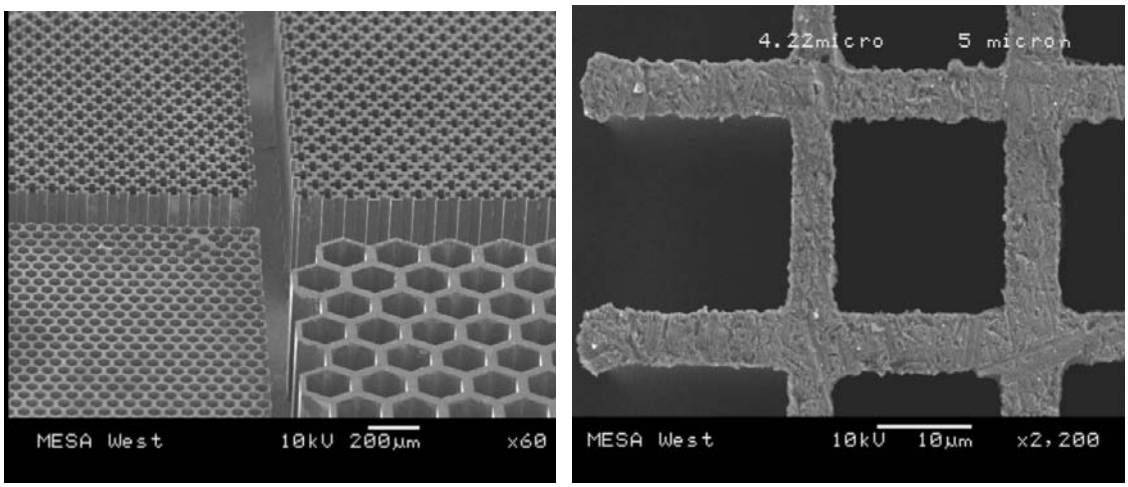

Fig. 2.3: 450 µm tall Nickel THz filters with grid sizes of 20-200 µm and wall thicknesses between 5 and 50 µm fabricated using the LIGA technique.

2.3 THz Photomixing Spectroscopy

In order to perform spectroscopy on filter elements and grating-gate detectors, a tunable continuous wave THz source was highly desired. Terahertz Photomixing Spectroscopy evolved from a desire to have a high resolution tunable spectrometer that performed at sub-mm wavelengths. At these wavelengths chemical identification can be performed where other portions of the spectrum do not see distinction. This can be attributed to rotational and vibrational resonances in molecules; essentially, in the THz, one can gain information about not just atomic composition, but also the arrangement of atoms. Therefore, by taking high resolution spectra at these frequencies, one can identify spectral fingerprints of chemicals that are not possible using other spectroscopic techniques. This has shown a great deal of promise in the field of homeland security where there is a need for an unobtrusive means of chemical detection at airports or train stations, for example.

2.3.1 Photomixing Theory

Photomixing relies on the concept of mixing two coherent high frequency sources onto a photoconductive emitter. The electromagnetic wave output of the photoconductive emitter (antenna, fig. 2.4) is dependant on the difference frequency (beat frequency) of the two coherent sources. This high

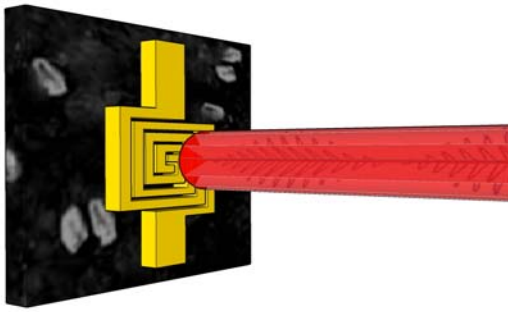

Fig. 2.4: Photomixer beams incident on a photoconductive emitter.

resistivity emitter is engineered to have electron-hole pair recombination times on the order of a picosecond. Electrodes to induce an electric field are then deposited on the surface of the high resistivity material. ErAs:GaAs photomixing antennas were used in this work. When illuminated, the incident photons (which exceed the bandgap energy of GaAs) generate electron-hole pairs within the emitter. The induced electric field generated by DC bias of the electrodes gives rise to a drift current of excess carriers within the material. It is the modulated temporal profile of these excess carriers generated by the photomixed beam on the electrodes of the antenna that creates THz radiation.

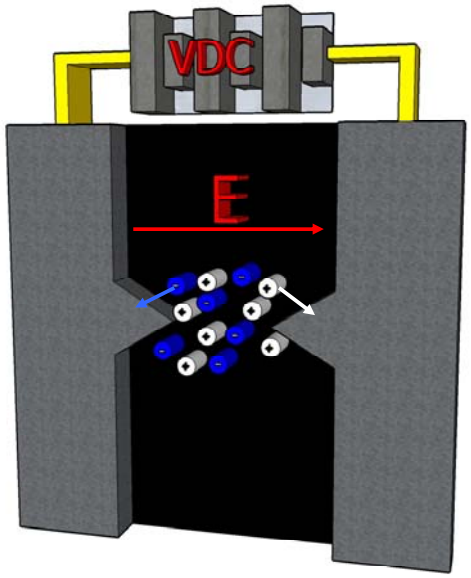

Fig. 2.5: Charge separation in an antenna from the applied DC electric field.

As was described before, the electromagnetic wave output of the photoconductive antenna is dependant on the difference or beat frequency of the incident beams. Consider two time (t) dependent electric fields

$$\mathbf{E_1} = E_0 \cos(\omega_1 t) \tag{2.1}$$

$$\mathbf{E_2} = E_0 \cos(\omega_2 t) \tag{2.2}$$

of same amplitude E_0 and differing frequencies $_1$ and $_2$. We define the beat frequency to be the difference between these two sources such that $_{beat}$= $_1$ - $_2$. Incident photons (with energy greater than the bandgap energy of GaAs) generate electron-hole pairs within the substrate of the GaAs material. Biasing the electrodes on the surface of the substrate generates an electric field which produces a drift current in the GaAs (fig. 2.5). This drift current (or photocurrent) is modulated at the beat frequency of the incident electromagnetic wave. This process is governed by the differential equations:

$$\begin{aligned} \frac{dn}{dt} &= G_e(t) - R_e \quad \text{(electrons)} \\ \frac{dp}{dt} &= G_h(t) - R_h \quad \text{(holes)} \end{aligned} \tag{2.3}$$

Where n and p are the electron and hole carrier concentrations, G is the generation rate, and R is the recombination rate. The generation rate, G, derived from the Poynting Vector is given by

$$G = \alpha \frac{P_{opt}}{\hbar \omega_p} \tag{2.4}$$

where is the absorption coefficient, ω_p is the carrier frequency of the mixed beam, and

$$P_{opt} = (E_1 + E_2)^2 \tag{2.5}$$

is the incident optical power. Expanding eq. 2.5, the optical power becomes

$$P_{opt} = E_0^2 \cos^2(\omega_1 t) + E_0^2 \cos^2(\omega_2 t) + E_0^2 \left[\cos\left((\omega_1 - \omega_2)t\right) + \cos\left((\omega_1 + \omega_2)t\right)\right]$$

$$P_{opt} = \underbrace{E_0^2 \cos^2(\omega_1 t) + E_0^2 \cos^2(\omega_2 t)}_{(a)} + \underbrace{E_0^2 \left[\cos(\omega_{beat} t) + \cos\left((\omega_1 + \omega_2)t\right)\right]}_{(b)} \quad (2.6)$$

where (a) is the contribution from the individual waves and (b) is created from the mixing of the two waves. The terms corresponding to direct oscillations at $_1$, $_2$, and their sum, are too fast for carrier generation to follow; the therefore only contribute a DC component to the photoconductivity. However, this is not the case for the difference frequency, $_{beat}$. For simplification we will concentrate only on the part of the expression that is dependant on the beat frequency, reducing (2.6) to

$$P_{opt} = E_0^2 \cos(\omega_{beat} t) \quad (2.7)$$

The generation rate then becomes

$$G = G_0 \cos(\omega_{beat} t)$$

where

$$G_0 = \alpha \frac{E_0^2}{\hbar \omega_p}$$

The recombination rate, *R*, is given by

$$R = \frac{n}{\tau} \quad \text{(for electrons)} \quad (2.8)$$

where *n* is the carrier density and is the recombination time. For electrons this gives

$$\frac{dn}{dt} = G_0 \cos(\omega_{beat} t) - \frac{n}{\tau}$$

A similar expression is given for holes. The solution to this differential equation is then

$$n(t) = \tau G_0 \frac{\left[\omega_{beat} \tau \sin(\omega_{beat} t) + \cos(\omega_{beat} t)\right]}{\omega_{beat}^2 \tau^2 + 1} + Ce^{\frac{-t}{\tau}} \quad (2.9)$$

where *C* is a constant derived from initial conditions. Shown in fig. 2.6 is a plot of the carrier density for three different recombination lifetimes. One can see from this plot that as the carrier recombination time increases the oscillatory term in the carrier density dies out. In order to have THz emission the recombination time must be $\tau \approx 1ps$ or less. Otherwise, the carrier modulation will be washed out. These ultra short lifetimes are characteristic of such materials as low-temperature grown GaAs and embedding GaAs with recombination centers such as ErAs.

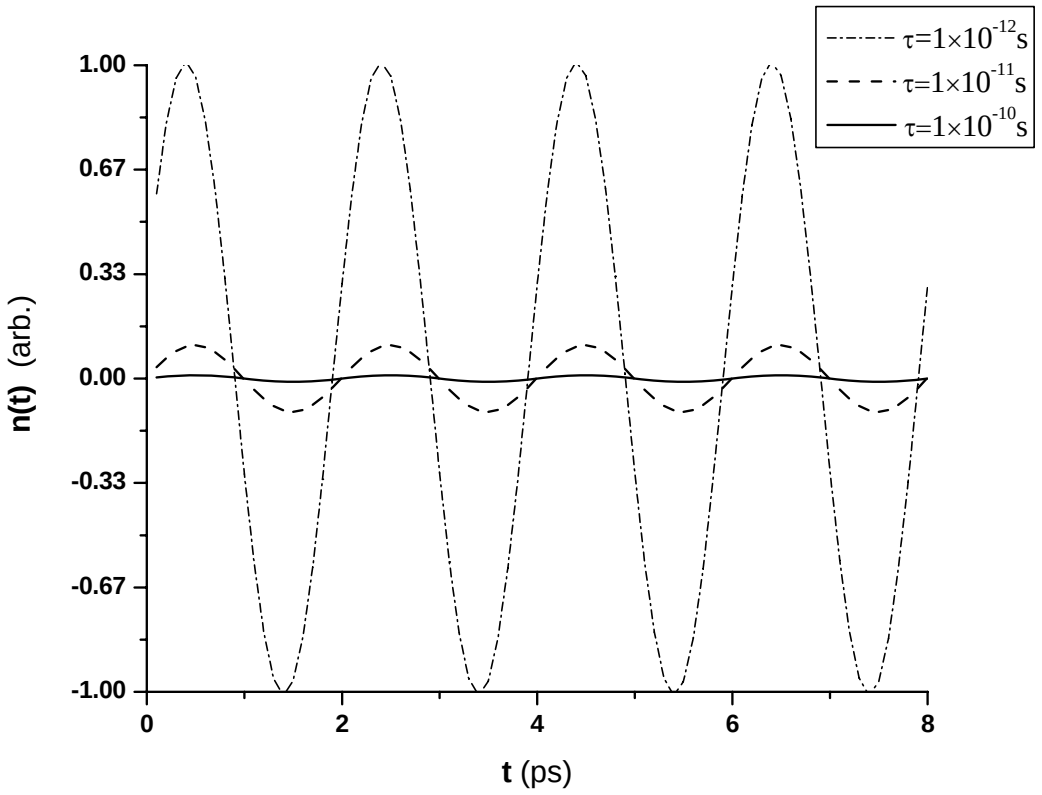

Fig. 2.6: Plot of Carrier Density for three different carrier lifetimes as a function of frequency. This plot shows that as the recombination time ( ) increases, the amplitude of the oscillatory part of the carrier density (n(t)) decreases.

2.3.2 Experiment Setup

The THz photomixing system used was designed to characterize plasmon resonance in grating-gate THz detectors. Shown in fig. 2.7 is a schematic diagram of the photomixing system used in these experiments. Two 100mW 780nm, tunable Littmann / Metcalf external cavity diode lasers purchased from Sacher Lasertechnik Group were used to generate the beat frequency. Laser 1 was locked to the Doppler broadened hyperfine structures in a Rb vapor cell as is diagramed in fig. 2.8. The hyperfine structures in Rb have a FWHM linewidth of ~6MHz . Side locking to a hyperfine structure provided stability stable within ~1MHz of = 780.246nm. The wavelength of laser 2 was monitored with a wavelength monitor that was accurate to 0.01 nm. This assured that the difference frequency between the two lasers was accurate when tuning the system to a specified frequency. Laser 2 was coarsely tuned by means

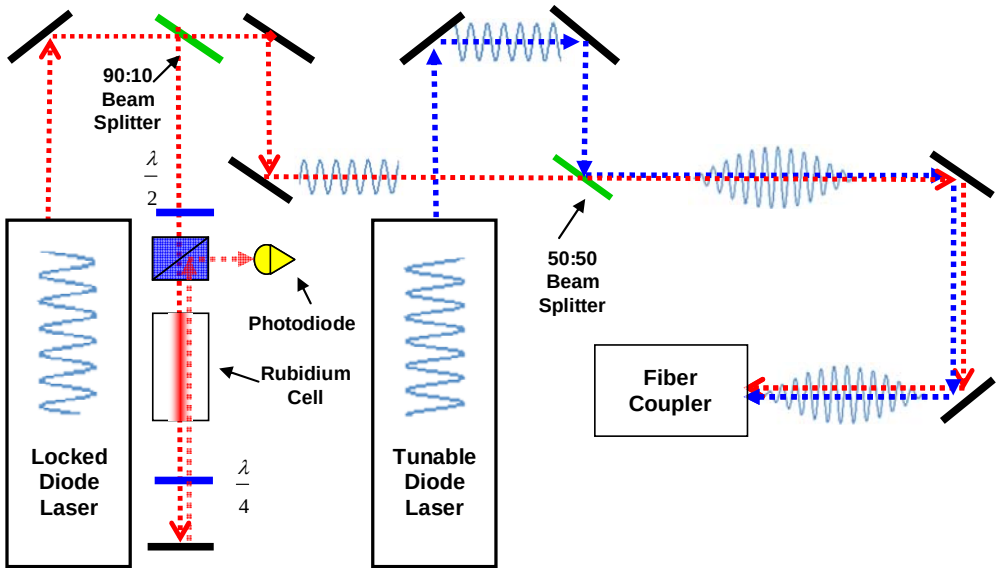

Fig. 2.7: Diagram of the system where the two diode lasers are overlapped and coupled into a single mode fiber. Coupling into a single mode fiber guarantees that the two beams are spatially overlapped before hitting the photoconductive emitter. Level 1 of the setup.

of a serial connection to a built in controller that changed the angular position of a grating on an electromechanical actuator. This provided up to 100GHz modehop free tuning range at 780nm as specified by the manufacturer. These laser systems do provide an option to finely tune the laser using an integrated piezo-electric stack with up to 50MHz resolution, but this option was not used because fine tuning was not needed for these particular experiments. The lasers were combined on a 780nm anti-reflection coated 50:50 beam splitter by pairs of dielectric mirrors. The joined laser beams were then focused onto a 780nm single mode fiber to assure that they were overlapped. This was verified by monitoring the contributed laser power of each on a photodiode power meter. By measuring the laser power in the fiber it was shown that there is a maximum ~ 30% coupling efficiency into the fiber at 780nm, thus allowing a coupling of ~32mW of laser power.

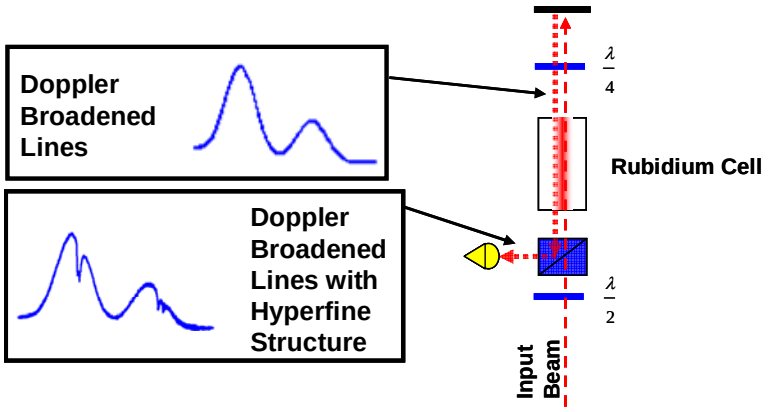

Fig. 2.8: Setup for saturated absorption spectroscopy of Rb used diode laser locking. Locking to a hyperfine structure in Rb provides laser stability to ~1MHz.

The THz photomixing system was constructed in a two level system. Both levels of the system were contained within a nitrogen purge box. The first level contained the photomixing optics to combine and monitor the two lasers. The second level was fiber coupled to the first level and contained the THz spectroscopy system (Fig. 2.9).

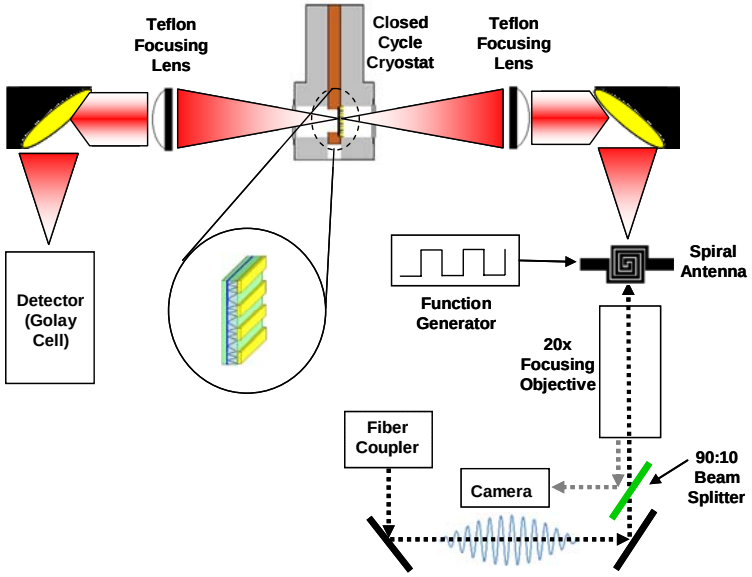

Fig. 2.9: System for THz spectroscopy. The overlapped beams are mixed in the photoconductive antenna to generate THz radiation. The THz radiation is passed through the sample mounted in a closed cycle cryostat and detected by a Golay cell. Level 2 of the setup.

The output of the fiber coupler was directed into a 20x Mitutoyo focusing objective that focused the combined beams onto the ErAs:GaAs photomixing antenna (Fig. 2.10).

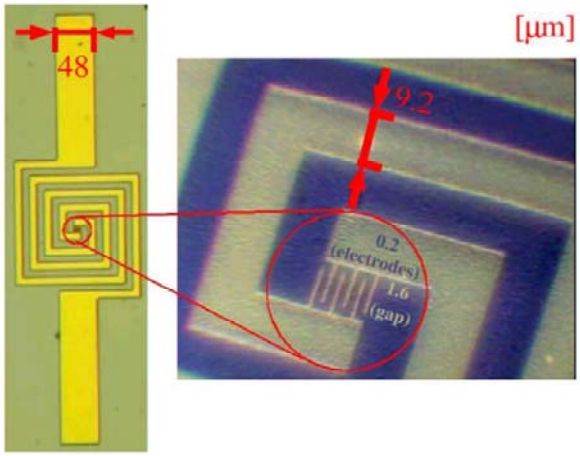

Fig. 2.10: Picture showing the structure of the photomixing antenna. The close up image shows the small gap interdigitated fingers that provide the large bandwidth tuning range of the photomixing system. Figure taken from [12].

The THz emission from the switch was coupled to free space through a hyperhemispherical silicon lens. The radiation pattern from a photoconductive antenna

by itself is highly divergent. The silicon lens reduces the divergence and aids coupling into free-space (Fig. 2.11). The THz emission was then collected and collimated in a

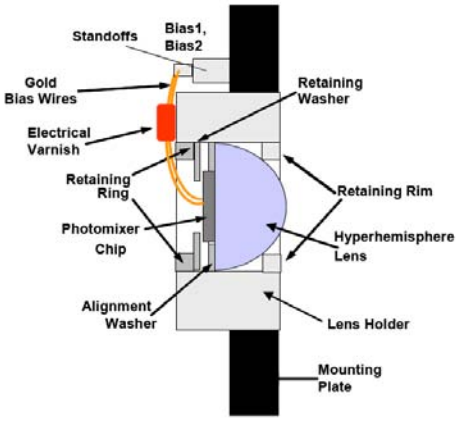

Fig. 2.11: Diagram showing the construction of the photomixing antenna. THz radiation is coupled into free space through a hyperhemispherical Si lens. Image courtesy of *Physical Domains, LLC.*

2 inch beam by a 2 inch diameter 6 inch focal length gold coated off-axis parabolic mirror ($f\#=3$). A 2" 100mm focal length Teflon focusing lens focused the beam through the sample and was then collected again by another 2" 100mm focal length Teflon lens and collimated. The collimated light was gathered by another 2" diameter 6" focal length gold coated off-axis parabolic mirror. The off-axis parabolic mirror focused the collected THz radiation into the 6mm aperture of a Golay Cell.

The Golay Cell detects THz radiation by the expansion of a noble gas within a cell (typically Xenon[13]). Heating caused by absorption of the THz radiation on a highly absorptive membrane with a mirror mounted on it causes the gas to expand within the cell and deflect a reference beam incident on a photocell inside the detector (Fig. 2.12). By moving the beam incident on the photocell the current which it produces changes. The change in current is monitored and is indicative of a change in THz radiation. Since Golay Cell detection relies on the expansion of a noble gas it does not differentiate between thermal emissions and THz radiation. Steps were taken to shield the Golay input aperture from all other radiating sources. The Teflon lenses provide a buffer

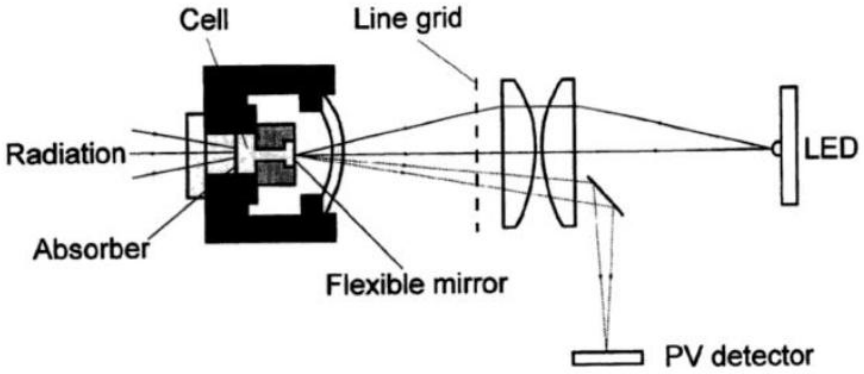

Fig. 2.12: Diagram of a Golay cell. Incident radiation causes the expansion of a gas cell, deflecting light emitted from a LED which is detected by a photovoltaic detector. Figure taken from [13]

between the thermal emission of the antenna and the input of the Golay Cell. The Golay Cell was calibrated with a molecular gas laser at 20Hz and was shown to have a responsivity of 4.66kV/W. This detector lacks the ability to measure the phase and polarization components of the THz beam. However, since these details were not necessary for our experiments, the Golay Cell was the ideal detector. Also, unlike most detectors for these wavelengths, such as a Si bolometer or a Hot Electron Bolometer, the Golay Cell does not require cryogens to operate.

A Stanford Research Systems lock-in amplifier was used to detect the output signal of the Golay Cell. The antenna bias was electrically chopped at 7Hz by a function generator with a 14V peak square wave output. Electrical chopping was chosen over optical chopping because it lowered the noise detected in the Golay Cell. The peak response of the Golay Cell used was found to be 7Hz for good signal-to-noise ratio (SNR), requiring a 1s integration time of the signal.

The sample was contained within a closed cycle helium system which allowed the sample to be cooled to a minimum of 8K. The cryostat was outfitted with clear mylar windows on either side of the sample. Black poly-ethylene was used to cover the windows of the cryostat to prevent ambient light from hitting the sample. Finally, a set of quartz windows covered with diamond particles (diamond scatter windows) were mounted in front and behind the sample. These windows were used because they are held at the cold-finger temperature in order to reduce their thermal emission. The helium cryostat was mounted on an X-Y translation stage configuration which was controlled by computer via a serial interface (Fig. 2.13). This allowed the sample to be scanned and imaged to locate its center. The output of the lock-in amplifier was collected by a data-acquisition system that was connected to a computer through an ethernet connection. Electrical connections to the sample were made via electrical feedthroughs in the cryostat and were controlled through the custom detector electronics.

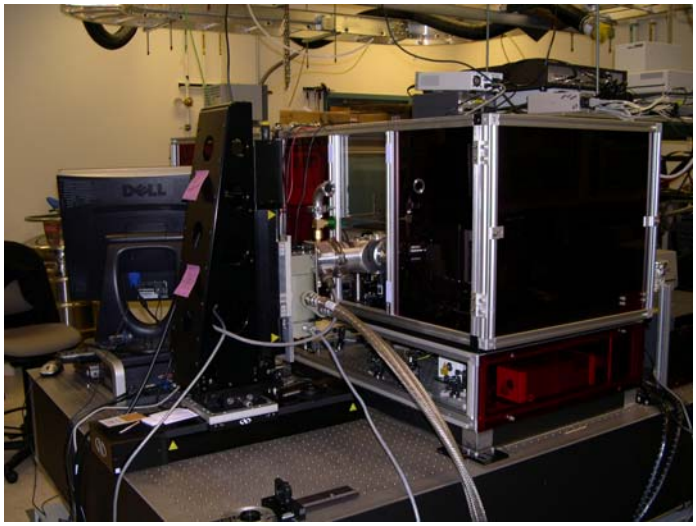

Fig. 2.13: THz Photomixing Spectroscopy system. This picture shows the closed cycle system mounted on XY translation stages and inserted into the nitrogen purge box. The laser mixing system is located below the THz spectroscopy system, the two are coupled by single mode fiber.

The computer system and software allowed for simultaneous control of the wavelength of the lasers, the position of the cryostat, the electrical bias and detection of the sample, and the output of the signal magnitude of the lock-in amplifier.

2.3.3 Characterization of LIGA waveguide filter

The photomixing system of section 2.3.2 was applied to characterize the filtering characteristics of a large area (1cm x 1cm) waveguide filter (section 2.2) which is pictured in Fig.2.14a. The filter spectrum, taken using the photomixer system of sec 2.3.2, is shown in Fig. 2.14b by placing the filter directly in front of the Golay cell. Clearly, the filter has a sharp turn-on and high-pass behavior that is in agreement with the predictions of sec 2.2.

Beyond using such elements as potential filters for broadband detectors, we have found this element to be particularly useful for characterizing photomixing systems of potential vendors. They are extremely robust in terms of sheer physical strength (so, hard to break), the filter is a room-temperature device, has a sharp turn-on, useful for resolution testing, and allows a specific amount of light to pass at high –frequencies (>600GHz). This element can also be scaled to move the turn-on point to even higher frequencies. This detail is particularly useful for upcoming work where we desire to characterize systems at frequencies >2THz.

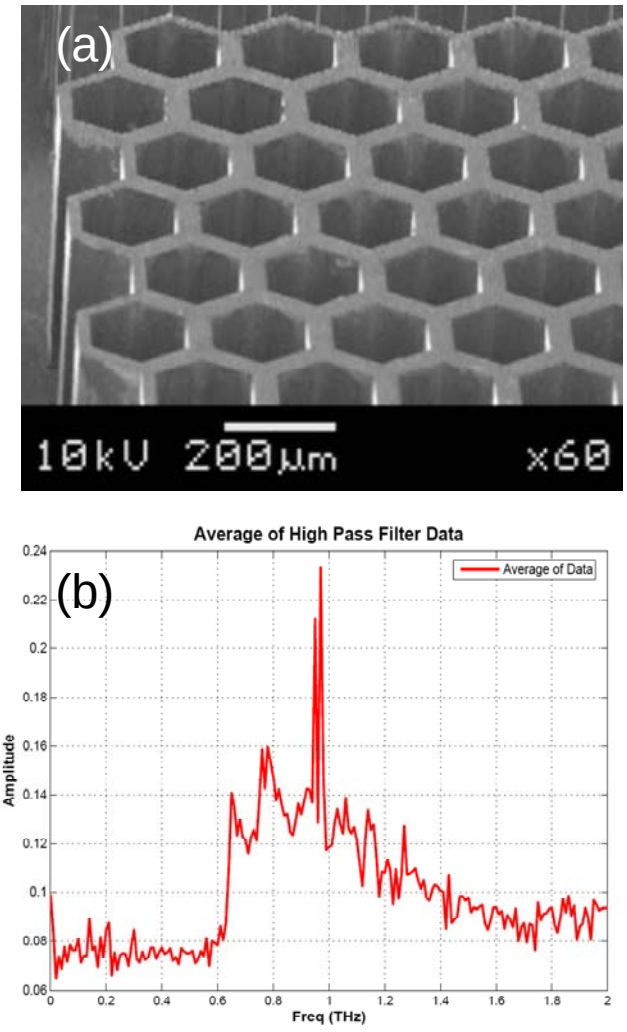

Fig. 2.14: LIGA waveguide filter. Filter image is shown in (a). Spectrum of filter transmission, taken with in-house photomixer system, is shown in (b).

2.3.3 Characterization of grating-gate detector

The grating-gate detector has a voltage tunable resonant photoresponse, and operates at normal incidence with little angular dependence. These traits, combined with realtively standard transistor processing, make it a good candidate for spectroscopic THz focal plane arrays. The current drawback is sensitivity. To address this, in the initial years of

this work (see sec 2.4 as well) we made engineering improvements to the detector. In the past year, using the photomixer setup of sec 2.3.2, we desired to measure the internal absorption efficiency of the detectors in order to determine where things currently stand, as well as identify where improvements can be made.

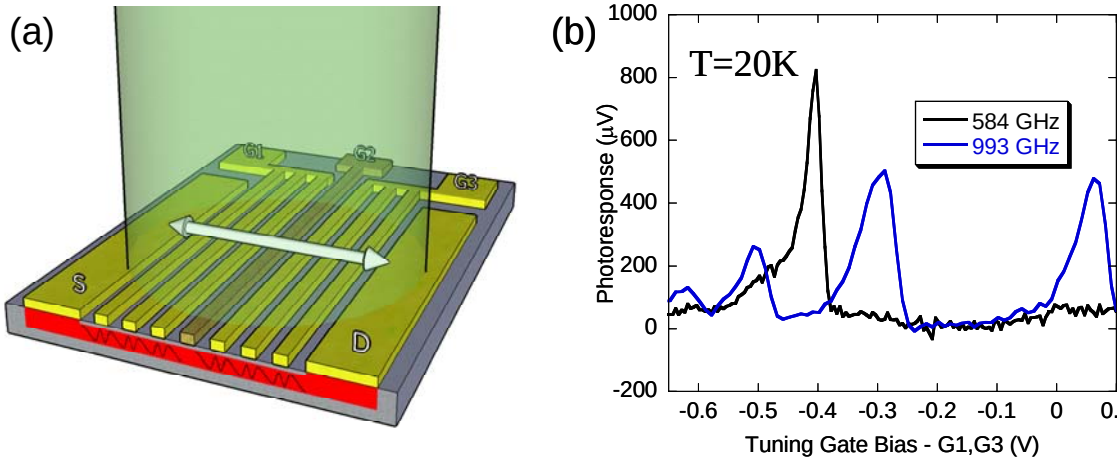

Fig. 2.15: The grating-gate detector. (a) shows the basic layout of the grating-gate detector. The device is fabricated from high mobility GaAs quantum well material. It has source (S) and drain (D) contacts, and spatially modulated gates G1, and G3 on the source and drain sides respectively. In between is a single gate line, G2, which is used to bias the device into a sensitive operating regime. In (b) an example of the spectral selectivity of the detector is shown as the device photoresponse is measured with 584GHz and 993GHz radiation from a far-infrared laser.

Observations of plasmon resonance shift with temperature have been observed in the range from 20K to 50K[5]. Experiments were performed at 20K, on a detector similar to that pictured in Fig. 2.15, where the plasmon photoresponse in this material was well characterized. The device was mounted on a cold finger inside of a continuous flow helium system and cooled to 20K. The cryostat was mounted on a translation stage (see sec 2.3.2) and an image was taken to identify peak center of the device (Fig. 2.16a). Measurements were made of the device's I-V characteristics without illumination to verify that the device was working properly. As voltage is increased towards pinch-off (V_g = -0.7) in the source-gate and drain-gate the device becomes more resistive due to depletion of carriers in the conduction channel (Fig. 2.16b,c). As the gates were ramped down data was taken to verify that the channel returned to equilibrium at V_g = 0V. Although this detector has three independent gates, for these transmission measurements, all gate lines were tied together to act as a single gate.

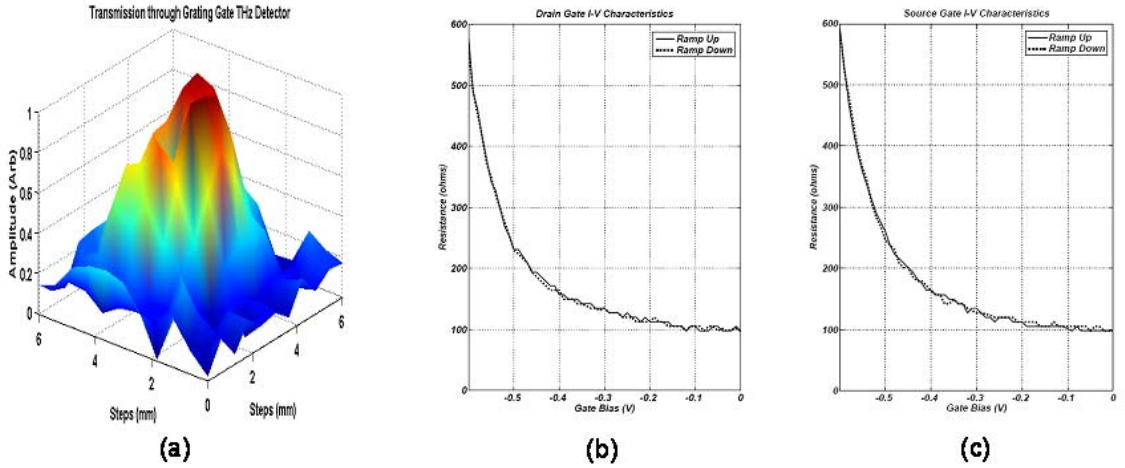

Fig. 2.16: Plots of the device characteristics (a) Transmission image of the sample in the cryostat (b) Drain-Gate IV Characteristics (c) Source-Gate IV Characteristics.

Transmission data was taken at three different frequencies and plotted as a function of the gate-bias voltage with the source and drain voltages at zero (Fig. 2.17). As the incident radiation is tuned towards higher frequencies the plasmon resonance is shifted towards less negative gate voltages. Local minima in the transmission spectrum identify locations of plasmon resonances within the quantum well.

Although transmission measurements may infer absorption, this does not paint the full picture. We have found evidence that more careful measurements must be made to attribute absorption strength to the local minima in the transmission spectrum. We consistently found that transmission did not return to the initial background transmission level with increased negative gate bias after peak plasmon resonance. This result implies one of two things:

1. Background absorption is different before and after plasmon resonance.

2. The amount of light reflected off the sample changes before and after resonance.

A change in background absorption is not consistent with photoresponse measurements, while a change in reflection due to changes in the index of the material is feasible for any material. Therefore, to truly understand this result, simultaneous measurements of both transmission through and reflection off the sample must be made.

From the design parameters of the grating-gated THz detector in Table 2.1 and eq. 1.1 we can calculate the ungated plasmon resonance. The plot in Fig. 2.17 shows that when the frequency of incident radiation is approximately equal to the ungated plasmon resonance (as given by the grating period and built in carrier density, approximate 430GHz) the amount of transmission is significantly less than at higher frequencies away from this resonance.

Table 0-1: Design parameters for grating-gated THz detector

Property	Value	Units (MKS)
Electron Density (n)	2.5×10^{15}	m^{-2}
Dielectric Constant ($_r$)	12.85	
Effective Mass (m^*)	$0.067\left(9.1\times10^{-31}\right)$	*Kg*
Electron Charge (*e*)	1.602×10^{-19}	*Coulomb*
Grating Period (δ)	4×10^{-6}	*M*

$$\mathbf{q} = \frac{2*\pi*n_q}{\delta} = \frac{2*\pi*1}{4\times10^{-6}m} = 1570796.3$$

$$w_p^2 = \frac{e^2 n\mathbf{q}}{2\varepsilon_o\varepsilon_r m^*} = \frac{\left(1.602\times10^{-19}\right)^2\left(2.5\times10^{15}m^{-2}\right)(1570796.3)}{2(12.85)\left(8.85\times10^{-12}\right)\left(0.067\left(9.1\times10^{-31}\right)\right)} \qquad (2.10)$$

$$w_p = 2.6959\times10^{12}\,rads$$

$$f_p = \frac{w_p}{2\pi} = \frac{2.6959\times10^{12}\,rads}{2\pi} \cong 430GHz$$

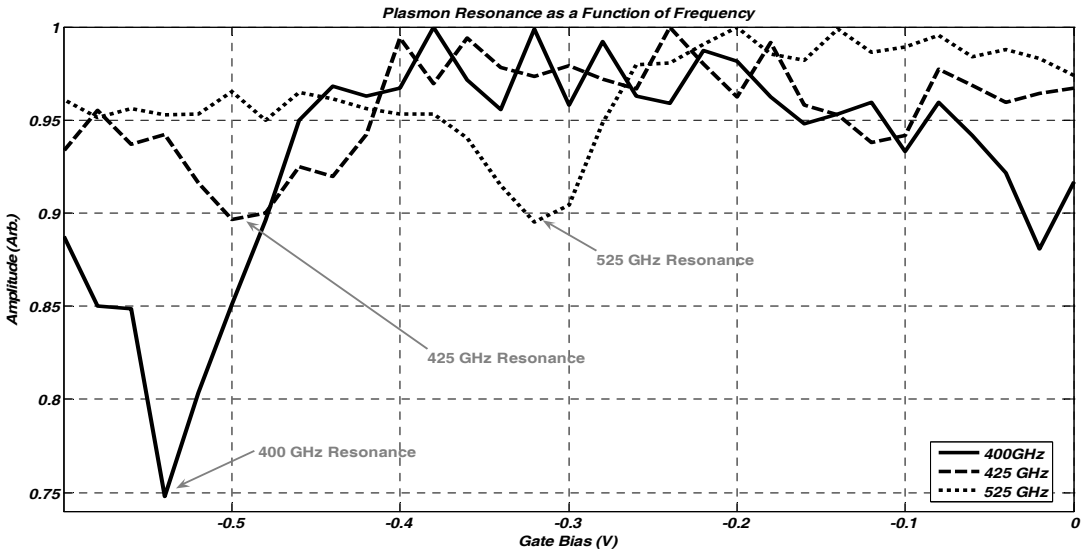

Fig. 2.17: Transmission through the grating-gated plasmon terahertz detector as a function of frequency. Local minima in the plot correspond to plasmon resonances at each frequency. Note that after resonance the transmission *does not* return to the original level.

Plasmon interactions between (ungated plasmons) the grating lines are different from those underneath (gated plasmons). Until now it was not understood how these different plasmons interrelate. As the frequency of the incident radiation approaches that of the ungated resonance, as shown in Eq. 2.10, there is apparently a strong coupling of both the

ungated and gated plasmons causing light transmission through the sample to be significantly lower than that seen at higher frequencies (Fig. 2.17). By changing the period of the grating the ungated plasmons resonance can be shifted to different frequencies. This allows detectors to be designed to have large plasmon resonances at different frequencies, modifying the peak operation of the detector. The bandwidth of this response is unknown at this time, but once found this may allow us to design broadly tunable detectors around the ungated plasmon resonance.

The plasmon resonances in these grating-gated terahertz plasmon detectors have been shown to be both electrically tunable and, in theory, infinite in number. Access to this large number of resonances demonstrates this device's usefulness in detecting terahertz radiation. It may be found in the future that particular plasmon modes persist to higher temperature while others may exhibit higher sensitivity. Through these experiments we have discovered that the properties of the detector change after the peak plasmon resonance. This result is most likely attributed to an index change in the material properties and needs to be investigated further. We have also shown that as we approach the ungated plasmon resonance of the detector there is apparently stronger coupling of the electromagnetic field to the plasmon resonance. As the ungated and gated plasmon resonances are brought into coincidence there is likely a strong coupling of the two different plasmons leading to increased absorption. Without investigating further it is unknown whether the reflectivity of the material changes as a function of frequency (as Fig. 2.17 implies). However, this phenomenon is common of resonances in dielectrics, metals, and semiconductors and is most likely the case for these detectors.

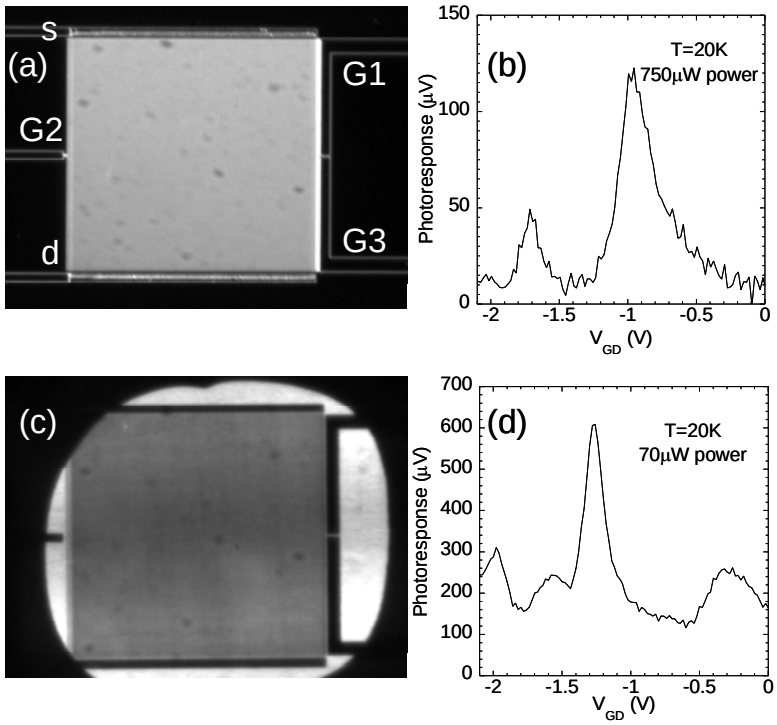

Fig. 2.18: Split grating-gate detectors made from double quantum well material. (a) The control device made on a thick substrate. Grating lines (not visible) run in the vertical direction. The contact pads for this device are several mm away from the detector which both eliminates antenna effects and allows for membrane isolation of the detector element. (b) The 'membrane' detector with backside illumination used to emphasize the area which has been etched out from behind the detector.

2.4 Membrane Style Split Grating-Gate Detector

By thermally isolating the grating-gate detector element[14], we have found a dramatic increase in pixel sensitivity is possible. In Fig. 2.18, two grating gate detectors, made from double quantum well material (made side-by-side from the same wafer EA1149) are highlighted. The photoresponses of these detectors to 750 W (thick detector) and 70 W (membrane detector) of 694GHz radiation are shown. Two things become apparent here. One is that the membrane detector is much more responsive that the standard detector. However, it also has apparently increased non-resonant absorption leading to a higher background level.

An important thing to understand about membrane isolation is how much one has slowed down the detector response. Basically, to implement a thermal isolation scheme, one is going to trade speed for improved sensitivity. In an attempt to understand the temporal response of the membrane isolated devices, new samples were made, both single and double quantum well, and sent to the pulsed FEL facility at UCSB for measurement by our collaborators. While work there is still underway, initial measurements have shown that the detectors still have s response speeds. If we consider that video rate applications can use ms pixel response times, this means that we still have approximately 3 orders of magnitude on speed that can be thrown away in order to achieve higher sensitivity. This being the case, membrane isolation may prove to be a winning scheme for achieving NEP < 10^{-10}W/ Hz in a focal plane array format.

2.5 Investigations of barrier behavior

The addition of an independently biased barrier gate has provided grating gate detectors with greater sensitivity (fig. 2.19, inset). The barrier gate is negatively biased with respect to ground to pinch-off and induces a barrier in the section of channel beneath it. Transport is thus controlled by thermal activation of carriers over this gate-controlled barrier. Because this voltage-induced barrier leads to highly temperature dependent, non-linear I-V characteristics, both a bolometric and a rectified response should be present.

Comparison of the detector response at 20 K and 100 K yields a consistent interpretation of the device physics producing a THz response.

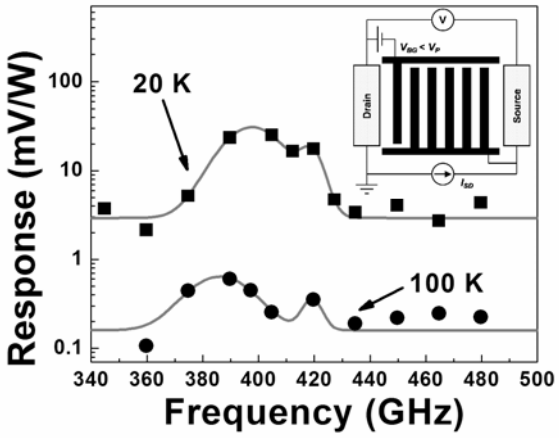

Fig. 2.19: Resonant terahertz response at 20 K (squares) with barrier gate bias V = -850 mV and source-drain bias I = -10 μA and at 100 K (circles) with barrier gate bias V = -815 mV and source-drain bias I = -75 μA. Inset: A schematic of the device and circuit.

Under similar bias conditions at both operating temperatures, the response shows a narrow resonance approximately 40 GHz wide (Fig. 2.19). Based on prior work with these devices and because in this bias scheme carriers below the grating gate move towards the barrier, we associate the resonant features illustrated here with the fundamental 2D plasmonic mode excited below the grating gate. The narrow width of the resonance at both temperatures suggests that the width of the resonance is not limited by the mobility, but perhaps by some other factor such as radiation damping.

Figure 2.20 illustrates the detector response with 420 GHz excitation for comparable bias conditions at 20 K and 100 K. The response at both temperatures tracks dV/dT, indicating the response is primarily bolometric in nature. The inset of fig. 2.19 demonstrates that the detector time constant follows the differential resistance dV/dI. Thus, the response time is a circuit time constant. The intrinsic response time is less than the circuit time constant at all bias point and therefore must be less than 0.5 s, the shortest detector time constant measured. This indicates that the response must then be a hot electron bolometric response from 20 K to 100 K.

Two important observations must be made concerning the amplitude of the response at these two operating temperatures. First, in both figure 2.19 and fig 2.20 the maximal response drops by approximately a factor of 50 from 20 K to 100 K. The response and dV/dT in fig 2.20 (a) and (b) have been scaled appropriately; we hypothesize this scale factor arises from a temperature-dependent energy relaxation time. The energy relaxation time should drop precipitously from 20 K to 100 K, severely reducing the bolometric response as well. Additionally, in fig 2.20 (b) the response has a positive amplitude for positive bias up to I = +60 μA. This is inconsistent with a bolometric response since dV/dT < 0 for all positive bias points. However, our analysis of the non-linear I-V characteristics indicates that a rectified response should have positive amplitude in this bias regime. This data suggests that the drop-off of the bolometric response at 100 K has revealed the rectified response, consistent with theoretical predictions.

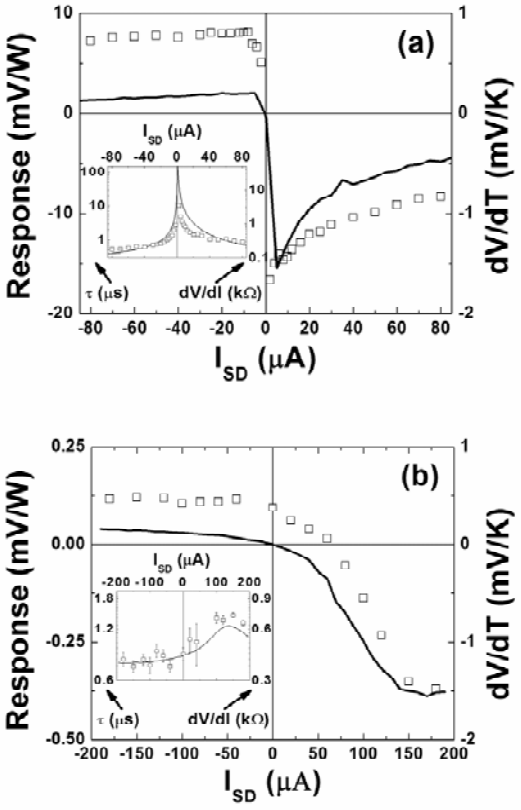

Fig. 2.20: Detector response (open squares) plotted with dV/dT (solid lines) at (a) 20 K and (b) 100 K as a function of source-drain current with fixed barrier gate bias V = -650 mV. The excitation frequency is 420 GHz. Inset: Response time constant (open squares) and device dV/dI (solid lines).

A rectified response would be

extremely beneficial from a device standpoint. Rectification is less sensitive to the operating temperature than the bolometric mechanism and would allow operation at or above liquid nitrogen temperatures. This opens up the possibility of optimizing the rectified response at elevated temperatures to engineer THz spectroscopic detectors with limited technology and cost overhead in the form of refrigeration.

3. CONCLUSIONS

While work under this project has seen an improvement in the grating-gate detector NEP from 10^{-5}W/ Hz to 10^{-8}W/ Hz, by the end of this work, we have found the necessary focus to be improving optical coupling (so, understanding plasmon absorption), and understanding the barrier behavior induced by the finger gate in the grating-gate detector. These are difficult issues to address, however both issues are well under way to being understood and there is a clear path laid out for future research.

In the final year of this research, much of the experimental focus was on THz photomixing and applying this technique to absorption measurements in the grating-gate detectors. To build up this effort, we learned how to design, build, and test our own photomixing components. We believe we now have the capability to build complete photomixing systems that are on-par, in not superior to, commercial systems. This expertise developed over the past year will be extremely valuable for follow on efforts involving THz spectroscopy of explosives and other materials.

4. References

1. J.H. Davies, *the Physics of Low Dimensional Semiconductors, An Introduction*. (Cambridge University Press, Cambridge, UK, 1998).
2. Tsuneya Ando, Alan B. Fowler, and Frank Stern "Electronic properties of two-dimensional systems". *Reviews of Modern Physics* **54**, 437 (1982).
3. S. J. Allen, D. C. Tsui, and R. A. Logan "Observation of 2-Dimensinoal Plasmon in Silicon Inversion Layers". *Phys. Rev. Lett.* **38**, 980-983 (1977).
4. X. G. Peralta, S. J. Allen, M. C. Wanke, N. E. Harff, J. A. Simmons, M. P. Lilly, J. L. Reno, P. J. Burke, and J. P. Eisenstein "Terahertz photoconductivity and plasmon modes in double-quantum-well field-effect transistors". *Appl. Phys. Lett.* **81**, 1627-1629 (2002).
5. E.A. Shaner, M. Lee, M.C. Grine, A.D. Grine, J.L. Reno, S.J. Allen, *Single-quantum-well grating-gated terahertz plasmon detectors*, Applied Physics Letters **87**, 193507 (2005).
6. M. Akazawa, Y. Yamazaki, E. Sano, "Terahertz Transmission Property of a Thing Metal Hole-Array Filter," JJAP, 44-49 (2005) L1481-1483.
7. C. C. Chen, "Transmission of Microwave Through Perforated Flat Places of Finite Thickness," IEEE Trans. Microwave Theory and Tech. 21-1 (1973) 1-6.
8. C. Winnewisser, F. Lewen, H. Helm, "Transmission Characteristics of Dichroic Filters Measured by THz Time-Domain Spectroscopy," Appl. Phys. A, 66 (1998) 593-598.
9. C. Genet, M. P. van Exter, J. P. Woerdmann, "Fano-type interpretation of red shifts and red tails in hole array transmission spectra," Opt. Commum. 225 (2003) 1938.
10. T. L. Willke, S. S. Gearhart, "LIGA Micromachined Planer Transmission Lines and Filters," IEEE Trans. Microwave Theory and Tech. 45-10 (1997) 1681-1688.
11. S. Biber, J. Schur, A. Hofmann, L.-P. "Schmidt, Design of New Passive THz Devices Using Micromachining Techniques," IEEE Proc. MSMW Symposium, (2004) 26-31.
12. J.E. Bjarnason, *Terahertz Photomixing Spectrometer Technology*, Ph.D. Dissertation, University of California Santa Barbara, (2007).
13. A. Rogalski, *Infrared Detectors* (Taylor and Francis CRC Press, Boca Raton, FL., 2000), p. 149.
14. E.A. Shaner, M.C. Wanke, A.D. Grine, S.K. Lyo, J.L. Reno, and S.J. Allen, *Enhanced responsivity in membrane isolated split-grating-gate plasmonic terahertz detectors*, Applied Physics Letters **90**, 1 (2007).

APPENDIX A: METRICS

- Publications
  - Far-infrared spectrum analysis using plasmon modes in a quantum-well transistor IEEE Phot Tech Lett 18: 1925-1927 SEP-OCT (2006)
  - Enhanced responsivity in membrane isolated split-grating-gate plasmonic terahertz detectors Appl Phys Lett, 90 181127 (2007)
  - Shaner, E. A., A. D. Grine, J. L. Reno, M. C. Wanke, S. J. Allen, *Plasmon Grating-Gate Devices have Potential as Tunable Terahertz Detectors*, Laser Focus World, Jan 2008.
  - Dyer, G. C., J. D. Crossno, G. R. Aizin, E. A. Shaner, M. C. Wanke, J. L. Reno, S. J. Allen, *A Plasmonic Terahertz Detector with a Monolithic Hot Electron Bolometer,* Journal of Physics: Condensed Matter, submitted 4/08.
- Proceedings
  - Tunable THz detector based on a grating gated field-effect transistor - art. no. 612006 P Soc Photo-Opt Ins 612006, (2006)
  - Shaner, E. A., A. D. Grine, S. K. Lyo, J. L. Reno, M. C. Wanke, S. J. Allen, *Electronically Tunable Plasmonic Grating-Gate Terahertz Detectors*, Proceedings of the SPIE Photonics East 2007, 9/9-12/07, Boston, MA.
- Invited Presentations
  - APS March Meeting, 2006
  - Princeton University Colloquium, Dec 2006
  - AVS Symposium, May, 2007
  - UMass Lowell, Sept, 2007
- Patents
  - "Electrically Tunable Terahertz Detector" TA# SD7957, Patent application 11/290,090
- Active Collaborations:
  - Jim Allen (UCSB)
  - Greg Aizin (CUNY, theory)
  - Physical Sciences Inc
  - Paul Planken (DELFT)

APPENDIX B: PROCESSING INFORMATION

Typical processing matrix for grating gate detectors:

A) Mesa Etch

1) Clean sample by spraying Acetone, IPA and blowing dry
2) Spin AZ5214 resist at 4000RPM/30seconds
3) Bake 90C/90second
4) Remove edge bead by exposing edges for 60seconds. Develop in AZ400K 1:4
5) Expose mesa pattern approximately 5.6 seconds in MJB3 aligner
    a. Mesa pattern must be aligned so that dovetail profile produced by etchant will be on the contact sides
6) Develop using AZ312 1:1.4 for approximately 35seconds
7) Descum in the LFE 5W O2 plasma for 5 minutes
8) Etch in H2SO4:H2O2:H2O 1:8:80 for approximately 50 seconds.
    a. Etch rate is approximately 100A/second. This etch is anisotropic and creats a smooth ramp along one crystal axis and a dovetail groove along the other. The dovetail side should be the corrugated side of the mesa where the contacts will be put down.
9) Clean in Acetone/IPA. Use Aceton spray gun if residual resist is present.

B) Ohmic contact

1) Repeat steps 1-7 of (A) using the 'ohmic' pattern
2) After descum and within 10 minutes before entering evaporation chamber, spray sample for 20 seconds with NH4OH:H2O2 1:20 solution and blow dry (no rinsing)
    a. This removes native oxide and oxide grown in descum
    b. Makes better contacts and also imrpoves metal sticking
3) Evaporate NiGeAuNiAu 80/270/540/140/1500 and liftoff in Acetone
    a. Use Acetone spray gun as needed

C) Gate Step (critical features)

1) Repeat steps 1-6 of (A) using 'Gate' pattern
    a. Don't do the descum, it is not known how that impacts device performance
2) Evaporate Ti/Au 200/500 and liftoff
    a. Soak in Acetone for about ½ hour or more to loosen everything up
    b. Finish with Acetone spray gun

D) Bonding Pads

1) Repeat steps 1-6 of (A) using the 'Pads' pattern
2) Evaporate Ti/Au 200/2000
3) Liftoff in Acetone

Special process for membrane devices:

1) Use crystal bond wax to mount sample face down to a glass slide
2) Spin 5214 resist on the back of the sample
3) Expose and develop a square over the detector using the backside aligner

4) Apply crystal bond wax around the sample edges and on the backside of the sample outside the perimeter of the exposed square
5) Use H2SO4:H2O2 1:4 to etch approximately 550 microns of the substrate
    a. This etchant is CONCENTRATED!
    b. Etch rate about 4 microns per minute. Initial etch rate about 10 microns/minute for the first 100 microns
    c. Use a profiler to measure etch depth, or start a dummy piece 20 minutes prior and wait for that to disappear
6) Rinse sample
7) Mix Citric Acid (1gm/ml):H2O2 ratio 4:1
8) Etch sample until the etch stop layer is reached
9) For unmounting, place the sample at an angle in a beaker of acetone. Eventually, it will slide off
    a. This technique has not caused any membrane fractures. There may be better ways to remove the crystal bond wax, but this works.
10) Place the sample in a beaker of IPA to rinse, then spray it off gently.

Distribution

1	MS0123	D. Chavez, LDRD Office	1011
1	MS1082	M.C. Wanke	1725
1	MS1082	J.J. Hudgens	1725
1	MS1082	A.D. Grine	1725
1	MS1082	T.A. Barrick	1725
1	MS1086	Dan Barton	1123
1	MS1303	J.L. Reno	1132
1	MS1415	E.A. Shaner	1123
1	MS1415	S.K. Lyo	1123
1	MS1421	J.A. Simmons	1120
1	MS1427	J.M. Phillips	1100
1	MS0899	Technical Library	9536 (electronic copy)


Sandia National Laboratories